Pergamon

Geochimica et Cosmochimica Acta, Vol. 68, No. 8, pp. 1735–1748, 2004

0016-7037/04 $30.00 + .00

doi:10.1016/j.gca.2003.10.010

The effect of dissolved barium on biogeochemical processes at cold seeps

Giovanni Aloisi,[1,*] Klaus Wallmann,[1] Sandra M. Bollwerk,[1] Alexander Derkachev,[2] Gerhard Bohrmann,[1] and Erwin Suess[1]

[1]GEOMAR-Research Centre for Marine Geosciences, Wischhofstr. 1-3, D-24148 Kiel, Germany
[2]Pacific Oceanological Institute, Far Eastern Branch of the Russian Academy of Sciences, POI, 43, Baltiyskaya Street, 690041 Vladivostok, Russia

(*Received July* 24, 2003; *accepted in revised form October* 9, 2003)

Abstract—A numerical model was applied to investigate and quantify the biogeochemical processes fueled by the expulsion of barium and methane-rich fluids in the sediments of a giant cold-seep area in the Derugin Basin (Sea of Okhotsk). Geochemical profiles of dissolved Ba^{2+}, Sr^{2+}, Ca^{2+}, SO_4^{2-}, HS^-, DIC, I^- and of calcium carbonate ($CaCO_3$) were fitted numerically to constrain the transport processes and the kinetics of biogeochemical reactions. The model results indicate that the anaerobic oxidation of methane (AOM) is the major process proceeding at a depth-integrated rate of 4.9 μmol cm^{-2} a^{-1}, followed by calcium carbonate and strontian barite precipitation/dissolution processes having a total depth-integrated rate of 2.1 μmol cm^{-2} a^{-1}. At the low seepage rate prevailing at our study site (0.14 cm a^{-1}) all of the rising barium is consumed by precipitation of barite in the sedimentary column and no benthic barium flux is produced. Numerical experiments were run to investigate the response of this diagenetic environment to variations of hydrological and biogeochemical conditions. Our results show that relatively low rates of fluid flow ($<\sim$5 cm a^{-1}) promote the dispersed precipitation of up to 26 wt% of barite and calcium carbonate throughout the uppermost few meters of the sedimentary column. Distinct and persistent events (several hundreds of years long) of more vigorous fluid flow (from 20–110 cm a^{-1}), instead, result in the formation of barite-carbonate crusts near the sediment surface. Competition between barium and methane for sulfate controls the mineralogy of these sediment precipitates such that at low dissolved methane/barium ratios ($<$4–11) barite precipitation dominates, while at higher methane/barium ratios sulfate availability is limited by AOM and calcium carbonate prevails. When seepage rates exceed 110 cm a^{-1}, barite precipitation occurs at the seafloor and is so rapid that barite chimneys form in the water column. In the Derugin Basin, spectacular barite constructions up to 20 m high, which cover an area of roughly 22 km^2 and contain in excess of 5 million tons of barite, are built through this process. In these conditions, our model calculates a flux of barium to the water column of at least 20 μmol cm^{-2} a^{-1}. We estimate that a minimum of 0.44×10^6 mol a^{-1} are added to the bottom waters of the Derugin Basin by cold seep processes, likely affecting the barium cycle in the Sea of Okhotsk.

1. INTRODUCTION

Biogeochemical processes at cold seeps regulate sediment-ocean chemical fluxes and result in widespread authigenic mineralization. Much attention has been devoted to the microbial processes that consume methane because they mitigate ocean-atmosphere methane fluxes and thus play a major role in the global carbon cycle. At cold seeps, most of the methane is consumed anaerobically by a consortium of microorganisms which use sulfate as an oxidant in a process known as the anaerobic oxidation of methane (AOM) (Iversen and Jørgensen, 1985; Boetius et al., 2000):

$$CH_4 + SO_4^{2-} \Rightarrow HCO_3^- + HS^- + H_2O \qquad (1)$$

AOM is the biogeochemical process with the highest turnover rate at cold seeps and produces considerable amounts of carbonate alkalinity (Luff and Wallmann, 2003). As a result, supersaturation with respect to carbonate minerals is rapidly attained in surface sediments, leading to the precipitation of authigenic carbonates:

$$Ca^{2+} + 2HCO_3^- \Leftrightarrow CaCO_3 + CO_2 + H_2O \qquad (2)$$

Carbonates formed through AOM occur as crust pavements which are exposed at the seafloor by erosion or gravitational processes and as massive build-ups which extend for up to tens of meters above the seafloor. These features cover large portions of the seafloor in virtually all known cold-seep areas world-wide (e.g., Paull et al., 1992; Faugères et al., 1997; Greinert et al., 2001; Aloisi et al., 2002).

Fluids expelled at cold seeps may also contain high amounts of dissolved barium, resulting in significant sediment-ocean barium fluxes (Torres et al., 1996a, 2002; Aquilina et al., 1997). Such fluxes impact significantly the modern barium cycling of semienclosed marine basins (Torres et al., 2002) and may have affected the global marine barium cycle in the geological past (Dickens et al., 2003). Barium dissolved in cold seep fluids is thought to originate from the dissolution of barite ($BaSO_4$) below the depth of sulfate depletion of marine sediments (Torres et al., 1996b; McManus et al., 1998). In support of this hypothesis, cold seepage of barium-rich fluids has been reported only from sedimentary basins overlain by biologically highly productive water columns where 'marine barite', which forms within microenvironments of decaying biologic debris (Dehairs et al., 1980; Bishop, 1988), is abundant.

* Author to whom correspondence should be addressed (valoisi@geomar.de).

The presence of dissolved barium at cold seeps complicates this generally carbonate-dominated diagenetic environment. It is thought that at relatively gentle fluid expulsion regimes, barium comes in contact with downwards-diffusing seawater sulfate in the sediment, resulting in the precipitation of authigenic barite (Torres et al., 1996a; Aquilina et al., 1997):

$$Ba^{2+} + SO_4^{2-} \Leftrightarrow BaSO_4 \quad (3)$$

This process is evoked to explain a wide variety of cold seep barite precipitates formed in the sediment including discrete crusts and nodules, as well as dispersed concretions and microcrystalline phases, associated to authigenic carbonates formed through AOM (Suess et al., 1998; Derkachev et al., 2000). Relatively more vigorous fluid expulsion regimes result in significant benthic barium fluxes. In this case, barium comes in contact with bottom waters and barite precipitates above the sediment-water interface. Barite chimneys ascribed to this process have been described from the San Clemente Basin (Torres et al., 2002), the Peru Margin (Dia et al., 1993; Aquilina et al., 1997; Torres et al., 1996a), the Monterey Canyon (Naehr et al., 2000), the Gulf of Mexico (Fu et al., 1994) and the Sea of Okhotsk (Greinert et al., 2002).

Although the conceptual model proposed by Torres et al. (1996a) and Aquilina et al. (1997) likely provides a correct qualitative description of this complex diagenetic system, a quantitative understanding of the biogeochemical processes involved is lacking. In particular, it is evident that the relative importance of barite chimney formation versus barite sediment diagenesis may vary from site to site. For example, chimney formation is particularly impressive in the Sea of Okhotsk where chimneys up to more than 20 m high cover large portions of the seafloor and, to a lesser extent, in the San Clemente Basin, whereas in the Gulf of Mexico, the Peru Margin, the Monterey Canyon and the Aleutian subduction zone (Suess et al., 1998) in-sediment diagenesis dominates over chimney formation. Furthermore, the amount of authigenic carbonate associated to barite varies from minor (San Clemente Basin) to very abundant (Peru Margin and Sea of Okhotsk). The biogeochemical and hydrological conditions favoring these different diagenetic regimes remain largely unknown. Moreover, because variable amounts of dissolved barium are lost through barite precipitation before they reach the water column, these different diagenetic regimes likely regulate sediment-ocean barium fluxes in distinct ways and could represent an important, albeit poorly constrained, aspect of the marine barium cycle.

To address these questions we conducted a pore water geochemical study of the giant cold seep area of the Derugin Basin in the Sea of Okhotsk. We developed a numerical model that simulates the biogeochemical processes taking place at barium-rich cold seeps. We apply this model to the Derugin Basin cold seep area to determine the dominant biogeochemical processes at barium-rich cold seeps, the conditions that favor barite chimney formation versus sediment diagenesis, the controls on the mineralogy of authigenic precipitates, and the magnitude of barium fluxes to the water column at the different diagenetic regimes.

Our study provides the first quantitative assessment of the effect of dissolved barium in cold seep fluids on biogeochemical processes and provides the basis for future studies of the role of cold seepage on the marine barium cycle.

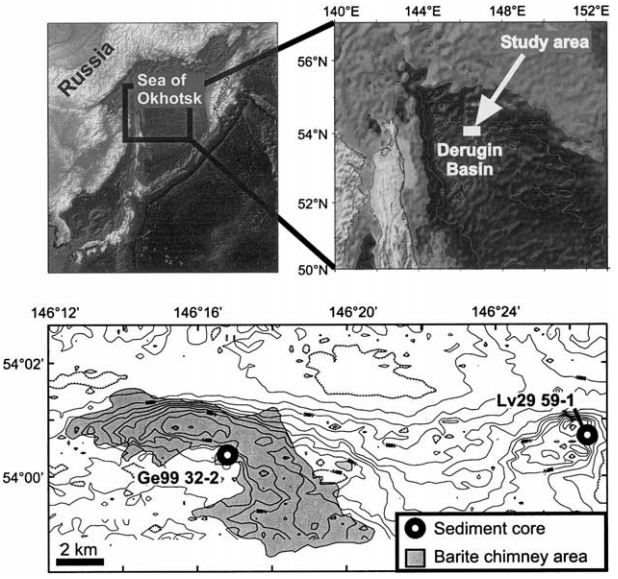

Fig. 1. Location of the study area and extent of the seafloor covered by authigenic barite chimneys.

2. DERUGIN BASIN COLD SEEP AREA

The Derugin Basin lies at a depth of ~1700 m in the western, deepest part of the Sea of Okhotsk (Fig. 1). The uppermost Neogene-Quaternary sediments of its several kilometers thick sedimentary succession are composed mainly of diatomaceous and radiolarian oozes reflecting the high productivity of the Sea of Okhotsk (Koblenz-Mischke, 1967; Bogorov, 1974). In its eastern flank, the Derugin Basin is characterized by NW-SE trending horst and graben structures. One of the horst structures is the locus of a widespread emission of methane- and barium-rich fluids which gives rise to spectacular diagenetic manifestations (Astakhova, 1993; Derkachev et al., 2000; Greniert et al., 2002). Barite chimneys up to 20 m in height composed of pure, porous (~40%) strontian barite (hereafter: barite) cover large portions of this horst (Fig. 2a) and are separated by stretches of flat seafloor where dense chemosynthetic-based benthic communities of clams document the emission of methane-rich fluids (Fig. 2b). Based on a detailed echosounder survey and on extensive video observations, we estimate that barite chimneys cover an area of approximately 22 km^2 and contain at least 5 million tons of barite (unpublished results of the Komex LV29 expedition). This is by far the biggest cold seep barite accumulation that has been reported and is comparable in mass to the largest barite deposits formed through high temperature hydrothermal processes (U.S. Geological Survey, 2003). Precipitation of authigenic minerals is not restricted to the water column. Sediment cores taken from the barite chimney area very often contain mixed barite-carbonate crusts at various sediment depths. In addition, mm- to cm-sized tubular structures composed either of authigenic Mg-calcite, authigenic barite or a mixture of these minerals, as well as Mg-calcite concretions and dispersed barite crystals, are common in these sediments. These authigenic phases are immersed in the diatom-and radiolarian-bearing siliceous oozes which form the bulk of sediments in the Derugin Basin. Sediment cores ob-

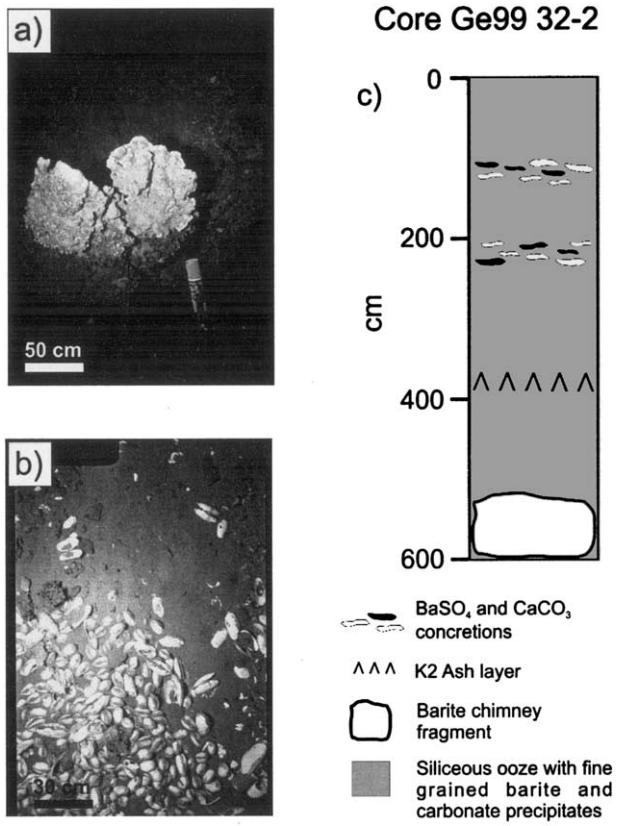

Fig. 2. (a) Photograph of two barite chimneys roughly 3 m in height. The surrounding seafloor is covered by authigenic barite and carbonate crusts. (b) Chemosynthesis-based benthic community of *Calyptogena* clams on a flat stretch of seafloor in the barite chimney area. (c) Lithological log of sediment core GE99 32-2.

tained from portions of the seafloor adjacent to barite chimneys also contain detrital barite, in the form of sandy layers or discrete barite bodies, which derives from the erosion of barite chimneys. This pattern of sedimentation and diagenesis has been observed in a large number of cores obtained from the barite chimney area during several cruises of the Komex project (Derkachev et al., 2000; Bollwerk et al., 2002). Both the authigenic barite forming the chimneys and that precipitating in the sediment are enriched to various degrees in ^{34}S and ^{18}O compared to seawater sulfate (Greinert et al., 2002). This is a strong indication that the barite sulfate originates from the residual sulfate pool remaining after bacterial sulfate reduction and provides a robust means of distinguishing this cold seep barite deposit from hydrothermal barite accumulations (Paytan et al., 2002). Moreover, the barite-associated authigenic carbonates are strongly depleted in ^{13}C (Greinert et al., 2002), indicating that they incorporate methane-derived carbon and showing that sulfate reduction is coupled to AOM.

Core GE99 32-2 (54°00.441′N, 146°16.916′E, 1510 m water depth) (Fig. 2c), taken from the barite chimney area (Fig. 1), offers a good example of the authigenic and sedimentary lithologies occurring in sediments influenced by seepage of barium- and methane-rich fluids. The lithological features of interest in this core are two 1 and 10 cm-thick authigenic barite-carbonate crust layers at 115 and 210 cm depth, respectively, and a 60 cm thick barite debris layer at the base of the core. The sediment is otherwise composed of Quaternary siliceous oozes rich in small-sized (mm to cm) detrital barite fragments and authigenic barite-carbonate precipitates of the kind described above. Core LV29 59-1 (54°00.765′N, 146°26.054E, 1425 m water depth), taken on a mound east of the major barite chimney area (Fig. 1), contains typical Quaternary siliceous oozes, is not affected by fluid seepage and is used as a reference core to investigate diagenetic processes unrelated to cold seepage taking place in the pelagic sediments of the Derugin Basin.

Although we present the pore water geochemistry of only two cores in this paper, we are confident that they are representative for the whole of the Derugin Basin. During three cruises to this area we sampled a total of 10 cores. Most cores showed no deep fluid signature but only the effects of early diagenesis. Their chemistry is very similar to the reference core presented in this paper. A few other cores showed a small admixture of deep fluids. The composition of the deep fluid component found in these cores is very similar to the composition of fluids at the base of core GE99 32-2. We decided to focus on core GE99 32-2 because we recovered almost pure deep fluids at the base of this core which we believe are representative for the whole Derugin Basin area.

3. SAMPLING AND CHEMICAL ANALYSIS

Coring was carried out with a 6 m long gravity corer. After recovery, sediment cores were split on deck and rapidly subsampled. Pore water extraction by squeezing was carried out in the on-board laboratory which was cooled at 4°C to prevent heating. Pore waters were analyzed on board for dissolved ammonia and sulfide using standard photometric procedures. Total alkalinity was determined by titration immediately after pore water separation. The remaining pore waters were later analyzed in the shore-based laboratory for dissolved anions (SO_4^{2-},I^-) and dissolved elements (Ba, Ca, Sr) using ion chromatography and optical ICP, respectively. Subsamples for dissolved Ca analysis were acidified immediately after squeezing to prevent further $CaCO_3$ precipitation. Total carbon, organic carbon and organic nitrogen were determined using an element analyzer. All analytical procedures applied on board of research vessels and in our GEOMAR laboratories are documented in detail at http://www.geomar.de/zd/labs/labore_umwelt/MUG.html.

4. BIOGEOCHEMICAL MODEL AND MODELING STRATEGY

To quantify the biogeochemical processes at barium-rich cold seeps, a numerical model based on the theory of early diagenesis of Berner (1980) was developed. The model considers AOM and barite and calcium carbonate precipitation/dissolution processes and accounts for Sr partitioning between fluids and barite. Based on the very limited amount of particulate organic carbon (POC)-related diagenesis at site LV29 59-1 (see below), we have not included POC-degradation processes in the model. The distribution of 12 chemical species (Ca^{2+}, Ba^{2+}, Sr^{2+}, HCO_3^-, CO_2, CH_4, HS^-, SO_4^{2-}, I^-, $CaCO_3$, $Ba_{(1-x)}Sr_xSO_4$ and $SrSO_4$) forced by fluid seepage, molecular diffusion, bioirrigation, burial and the above mentioned biogeochemical processes can be described by the

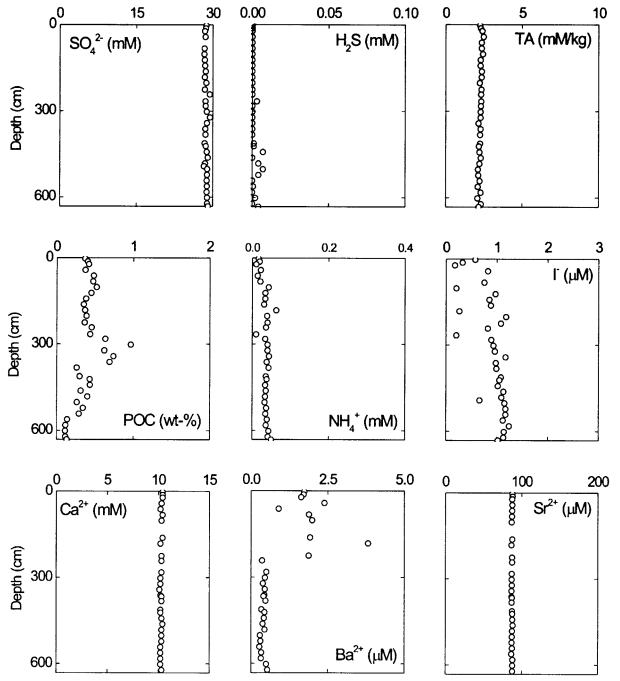

Fig. 3. Measured concentration profiles in the reference core LV29 59-1. First row: concentration of sulfate, sulfide and total alkalinity (TA). Second row: concentration of particulate organic carbon (POC), ammonia and iodide. Third row: concentration of calcium, barium and strontium.

model. The distribution of authigenic barite and calcium carbonate, as well as the importance of Ba^{2+} fluxes to the bottom waters can be investigated under a wide range of fluid chemistries and hydrological conditions which correspond to different diagenetic regimes, ranging from dispersed in-sediment diagenesis to barite chimney formation. A detailed description of the model is given in the Appendix.

Critical values of kinetic constants and other biogeochemical parameters were determined by fitting the model to the available biogeochemical data set of core GE99 32-2, providing a quantitative overview of the biogeochemical processes at the cold seeps of the Derugin Basin (section 5.1.2). This is the standard model run that serves as a starting point for the numerical experiments aimed at investigating the conditions favoring the development of barite chimneys (section 5.2.1), the controls on the mineralogy of authigenic precipitates (section 5.2.2) and the magnitude of barium fluxes to bottom waters (section 5.2.3).

5. RESULTS AND DISCUSSION

5.1. Biogeochemical Processes in the Sediments of the Derugin Basin

5.1.1. Sediments unrelated to fluid seepage (core LV29 59-1)

Pore water geochemical profiles in core LV29 59-1 indicate that the sediments of the Derugin Basin undergo only very limited diagenesis (Fig. 3). The concentration of sulfate throughout most of the core is equal to seawater values indicating negligible rates of sulfate reduction. The concentration of alkalinity also deviates very little from seawater values indicating that also other organic matter degradation processes are very limited. Consistently, the concentration of ammonia and iodide, which are both produced during organic matter degradation (Berner, 1980; Kennedy and Elderfield, 1987; Martin et al., 1993), increases very little downcore. Therefore, the variations in POC content of this core reflect varying organic matter fluxes and/or sedimentation rates, rather than POC consumption through degradation processes. Calcium and strontium concentrations are equal to seawater values throughout the core indicating that no carbonate precipitation/dissolution processes are taking place. Dissolved barium, instead, is relatively abundant and irregularly distributed in the upper 250 cm of the core. This could be due to barium release from organic matter or marine barite in suboxic (McManus et al., 1998) or anoxic microenvironments. Indeed, relatively elevated H_2S concentrations show that sulfate reduction occurs locally throughout the core.

5.1.2. Barium and methane seep site (core GE99 32-2)

Contrary to the reference site, the pore fluids in core GE99 32-2 show ample evidence of being affected by barium- and methane-related biogeochemical processes (Fig. 4). Sulfate is completely depleted at a depth of ~250 cm. This depth also corresponds to a maximum in sulfide concentration and of total alkalinity, and to the shallowest depth where methane is present in elevated concentration (>1 mM), indicating that AOM (Eqn. 1) is taking place in these sediments. Dissolved barium is present in high concentration (up to 1.85 mM) in the pore fluids of the lower part of the core. The concentration of barium decreases upcore and reaches seawater values close to the sulfate-methane boundary, indicating ongoing precipitation of barite (Eqn. 3) at the sulfate-methane boundary. A similar pattern in the strontium profile indicates that strontium is being incorporated in the precipitating barite. Moreover, calcium concentrations fall from seawater values at the top of the core, to roughly half this value at the sulfate-methane boundary, suggesting that calcium is being consumed at this depth by precipitation of calcium carbonate (Eqn. 2).

The numerical model introduced in section 4 was applied to quantify the biogeochemical processes taking place at site GE99 32-2. A standard model run was carried out to constrain the values of kinetic constants and other parameters of the diagenetic environment. In this run the simulation time was set to 2000 yr, after which the solute profiles attain near steady-state conditions which are controlled by the prevailing biogeochemical processes and are influenced by the presence of the barite debris layer. The same model run was brought into steady-state to investigate the steady-state distribution of solutes and solids under the same chemical and hydrological conditions. The good fit between the data (circles in Fig. 4) and the simulated profiles (solid and dashed lines in Fig. 4) demonstrates that the model can be used to simulate biogeochemical processes at site GE99 32-2. The concentration profiles of $CaCO_3$, dissolved iodide (I^-), sulfate (SO_4^{2-}), sulfide (HS^-), barium (Ba^{2+}), strontium (Sr^{2+}), calcium (Ca^{2+}) and of total alkalinity (TA) are well reproduced by the model. A significant discrepancy is observed only for dissolved methane (CH_4) and calcium carbonate ($CaCO_3$); the former is due to loss of meth-

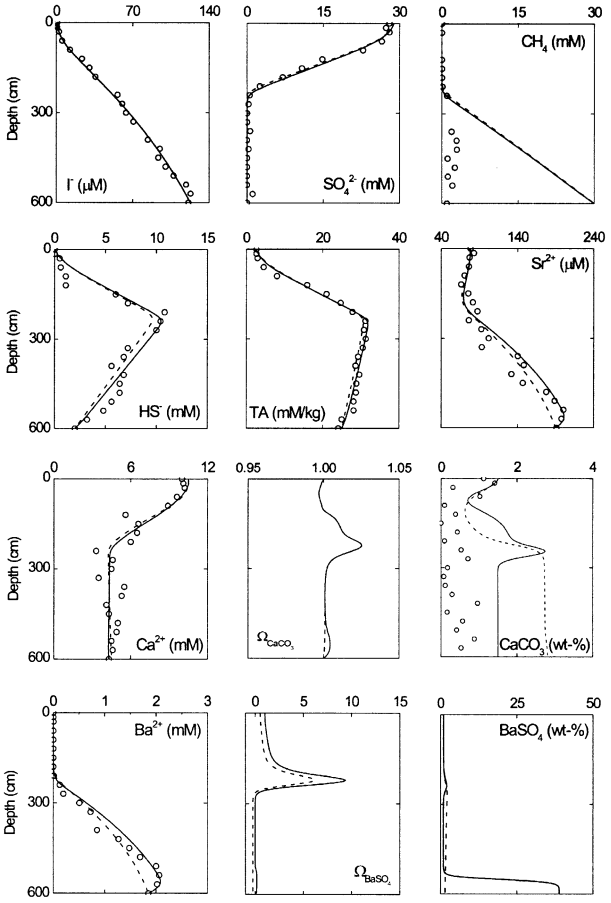

Fig. 4. Simulated and measured concentration profiles from core GE99 32-2. First row: concentration of iodide, sulfate and methane. Second row: concentration of sulfide, total alkalinity (TA = HCO_3^- + HS^- in model profile) and strontium. Third row: concentration of calcium, saturation state with respect to calcium carbonate and concentration profile of calcium carbonate. Fourth row: concentration of barium, saturation state with respect to barite and barite concentration curve. Simulated steady-state profiles are plotted as dashed lines, non–steady state profiles are plotted as solid lines and measured concentrations are plotted as circles, where available.

ane from the sediment by degassing during sample retrieval, the latter to the fact that calcium carbonate profiles are calculated for present turnover rates while the data reflects the dynamic history of calcium carbonate accumulation. Values of parameters constrained by fitting the model results to pore water data from core GE99 32-2 are listed in Table 1. Values of other variable parameters and boundary conditions used in this model run are listed in Table 2.

Only minor amounts of iodide are produced through organic matter degradation processes at the reference site (see section 5.1.1). Fluids at the base of core GE99 32-2 contain orders of magnitude more iodide than those at the reference site implying that the iodide distribution in core GE99 32-2 is controlled by transport processes (advection, diffusion, bioirrigation) rather than reactions. Thus, dissolved iodide can be considered as a conservative constituent and can be used to constrain transport processes in core GE99 32-2. In core GE99 32-2, the I^- profile is concave downwards in its lower part and concave upwards in its upper part (Fig. 4), indicating that sediments are subject to mixing processes at both ends. The best fit to the field data was obtained allowing for a gentle upwards advection of fluids (0.14 cm a^{-1}) and for bioirrigation in the surface layers (Table 1). The constrained value of the kinetic constant for AOM, k_{AOM}, 1 cm^3 μmol^{-1} a^{-1}, is included in the range of values reported in the literature (Van Cappellen and Wang, 1996). The constrained value of the kinetic constant for calcium carbonate precipitation, k_{CPPT}, 100 μmol cm^{-3} a^{-1}, is one order of magnitude smaller than that constrained by Luff and Wallman (2003) for cold seeps of Hydrate Ridge. Values chosen for the kinetic constants for barite precipitation and dissolution, k_{BPPT} and k_{BDISS}, the parameters controlling the shape of the initial barite profile, $(Ba,Sr)SO_{4sed}$, C_{dl}, and d_x, the mole fraction of Sr in preexisting barite, f_{Srpb}, and the fluid-barite Sr partition coefficient, P_C, result in a good fit of the Ba^{2+} and Sr^{2+} data (Fig. 4). The choice of a high barite concentration in the debris layer (40 wt% DS) is essential to reproduce the maxima of Ba^{2+} and Sr^{2+}. The determined value of f_{Srpb}, 0.045, corre-

Table 1. Parameter values determined by fitting the model to the biogeochemical data set of core GE99 32-2.

Data	Constrained parameter	GE99 32-2 (standard run)
I^-	w_0 (cm a^{-1})	0.14
I^-	BIO0 (a^{-1})	1
I^-	xs (cm)	3
SO_4^{2-}, HS^-	k_{AOM} (cm^3 μmol^{-1} a^{-1})	1
SO_4^{2-}, HS^-	C_{CH_4} (L,t) (μmol cm^{-3})	30
TA	$C_{HCO_3^-}$ (L,t) (μmol cm^{-3})	23
Ca^{2+}, $CaCO_3$	k_{CPPT} (μmol cm^{-3} a^{-1})	100
Ca^{2+}, $CaCO_3$	k_{CDISS}(a^{-1})	0.1
Ba^{2+}, Sr^{2+}	k_{BPPT} (μmol cm^{-3} a^{-1})	4×10^{-4}
Ba^{2+}, Sr^{2+}	k_{BDISS} (a^{-1})	9×10^{-6}
Ba^{2+}, Sr^{2+}	P_C (−)	50
Ba^{2+}, Sr^{2+}	$(Ba,Sr)SO_{4_{sed}}$ (wt-% DS)	1
Ba^{2+}, Sr^{2+}	C_{dl} (wt-% DS)	40
Ba^{2+}, Sr^{2+}	d_x (−)	5
Ba^{2+}, Sr^{2+}	f_{Srpb} (−)	0.045

Table 2. Values of variable parameters and variable boundary conditions used in the standard model run.[a]

Parameter/boundary condition	Core GE99 32-2 (standard run)
L (cm)	600
ϕ_0	0.95
ϕ_f	0.708
ϕ_a (cm^{-1})	0.0013
v_f (cm a^{-1})	0.011
C_{I^-} (L,t) (μmol cm^{-3})	0.123
$C_{Ca^{2+}}$ (L,t) (μmol cm^{-3})	4.3
$C_{Ba^{2+}}$ (L,t) (μmol cm^{-3})	1.85
$C_{Sr^{2+}}$ (L,t) (μmol cm^{-3})	0.14
C_{CO_2} (L,t) (μmol cm^{-3})	3.76
$C_{SO_4^{2-}}(L,t)(\mu molcm^{-3})$	0
C_{HS^-} (L,t) (μmol cm^{-3})	2
C_{CaCO_3} (0,t) (wt-% DS)	1.5
$C_{(Ba,Sr)SO_4}$ (0,t) (wt-% DS)	0.045

[a] The sedimentation rate, v_f, was obtained based on the depth of ash layer K2 (26800 yBP; Biebow et al., 2000) in core GE99 32-2.

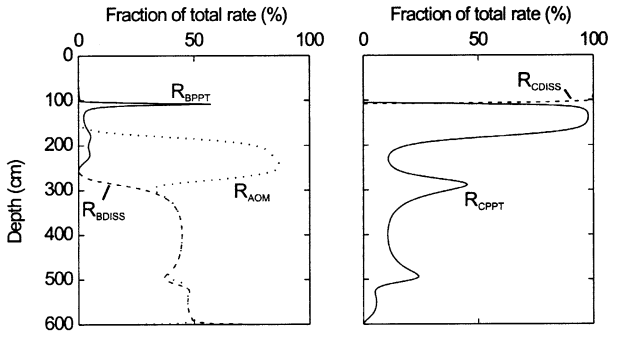

Fig. 5. Relative rate-depth profiles of the simulated biogeochemical processes at site GE99 32-2. Profiles are in near steady-state conditions (t = 2000 a) to account for the effect of the barite debris layer (core depth: 540–600 cm) on the biogeochemical processes at this site (see section 5.1.1). The depth-integrated values of the presented rates are summarized in Table 3. RBPPT = barite precipitation; RBDISS = barite dissolution; BCPPT = calcium carbonate precipitation; RCDISS = calcium carbonate dissolution; RAOM = anaerobic oxidation of methane.

sponds to a Sr concentration in the barite of ~2 wt% DS, which lies at the centre of the range of Sr concentrations determined on samples of barite chimneys from the Derugin Basin (Greinert et al., 2002). A significant discrepancy exists between the value of the Sr fluid-barite partition coefficient, P_C, and the theoretical value of this parameter for seawater. For seawater, P_C can be calculated as the ratio of the stoichiometric solubility products of Celestite, ${}^{Sr}K^*_{sp}$, and barite, ${}^{Ba}K^*_{sp}$ (Rushdi et al., 2000):

$$P_C = \frac{{}^{Sr}K^*_{sp}}{{}^{Ba}K^*_{sp}} \quad (4)$$

From tabulated thermodynamics data given in Rushdi et al. (2000), P_C for seawater salinity and a temperature of 5°C is equal approximately to 4200. The value of 50 that we obtain with the model is considerably smaller, possibly due to the difference in the chemistry of the cold seep fluids, in particular the Sr^{2+}/Ba^{2+} of fluids, compared to seawater (for which Eqn. 4 is valid), and/or to differences in the rate of barite precipitation in pore waters compared to seawater.

The rate-depth profiles calculated for site GE99 32-2 allow for a better understanding of the vertical zonation of biogeochemical processes at this site. Rates of single processes are normalized to the sum of all rates, to better recognize the dominant processes at each depth (Fig. 5). In the top 100 cm, calcium carbonate dissolution is the dominant process, accounting for up to 100% of the total rate. Deeper in the core, between 100 and 285 cm, calcium carbonate dissolution stops, while calcium carbonate precipitation and AOM become the dominant biogeochemical processes accounting for up to 97 and 90% of the total rate, respectively. The kinetics of barite precipitation is much slower than that of calcium carbonate precipitation. This is reflected in the very small kinetic constant for the former process compared to the latter (Table 1) and results in a supersaturation with respect to barite which is one order of magnitude greater than that with respect to calcium carbonate (Fig. 4). Nevertheless, at site GE99 32-2, all of the rising barium is consumed through precipitation of barite in the sediment column and no benthic barium flux is present. In the depth interval where AOM and carbonate precipitation occur, dissolved inorganic carbonate is produced (Eqn. 1 and 2). Because the neutral dissolved CO_2 molecule is surrounded by a smaller shield of water molecules than the charged HCO_3^- ion, CO_2 diffuses more rapidly than HCO_3^- (Boudreau, 1997). Differential diffusion produces undersaturation in the top 100 cm of the sediment column (Fig. 4) which drives the calcium carbonate dissolution in this interval. Below 285 cm dissolved sulfate is nearly absent, due to consumption through AOM (Fig. 4). Therefore, pore fluids are undersaturated with respect to barite, and, according to the model, barite dissolves (Fig. 4). Thus, between 285 cm and the bottom of the core, barite dissolution accounts for 35 to 45% of the total rate. While the liberated Ba^{2+} and Sr^{2+} are transported upwards to be reprecipitated as barite at the sulfate-methane boundary, the sulfate produced during barite dissolution is consumed in situ by AOM which accounts for 35 to 45% of the total rate in this depth interval. Although barite dissolution proceeds at a relatively elevated rate, dissolved sulfate is virtually absent due to AOM. Fueled by AOM, calcium carbonate precipitation takes place below 285 cm, accounting for less than 30% of the total rate.

Table 3. Depth-integrated rates of the dominant biogeochemical reactions at site GE99 32-2 (rates in μmol cm^{-2} a^{-1}).

Process	Symbol	Depth integrated rate
AOM	R_{AOM}	4.91
$CaCO_3$ precipitation	R_{CPPT}	0.94
$CaCO_3$ dissolution	R_{CDISS}	0.56
$(Ba,Sr)SO_4$ precipitation	R_{BPPT}	0.21
$(Ba,Sr)SO_4$ dissolution	R_{BDISS}	0.32

A quantitative comparison of the different biogeochemical processes at site GE99 32-2 is possible considering their depth-integrated rates calculated at t = 2000 a (Table 3). Biogeochemical turnover at site GE99 32-2 is dominated by AOM, proceeding with a depth-integrated rate of 4.91 μmol cm^{-2} a^{-1}, 2 to 3 orders of magnitude lower than at cold seeps where advection rates of 10 cm a^{-1} or higher bring the sulfate-methane boundary within 20 cm from the seafloor (Wallmann et al., 1997; Boetius et al., 2000; Luff and Wallmann, 2003). Calcium carbonate and barite precipitation/dissolution processes proceed at rates 5 to 20 times lower than AOM. Similar ratios of AOM rates to calcium carbonate precipitation rates were also found for cold seeps at Hydrate Ridge (Cascadia Margin) (Luff and Wallmann, 2003). The fitting procedure constrains a methane concentration of 30 mM at the base of the core (Fig. 4). This value is lower than the saturation concentration with respect to gas hydrates (60 mM at site GE99 32-2; Zatsepina and Buffet, 1997), so that gas hydrates are not expected to be present in surface sediments at this site. Nevertheless, the methane flux from below is sufficiently large in order for AOM to be the dominant biogeochemical process in the investigated depth interval.

5.2. Numerical Experiments

5.2.1. *Conditions favoring barite chimney formation versus sediment diagenesis*

In a first set of model runs, the seepage rate was increased from 0.14 to 300 cm a^{-1} which covers the range of seepage

rates responsible for carbonate crust formation at cold seeps (up to 90 cm a^{-1}; Luff et al., submitted) and extends it into the domain of seepage rates which produce important benthic methane fluxes (>100 cm a^{-1}; Luff and Wallmann, 2003). The effect of the seepage rate on the depth-integrated rates of AOM and of calcium carbonate and barite precipitation, as well as on the concentration profiles of the two minerals in the sediment, was investigated. In addition, to understand the conditions favoring barite chimney formation, the benthic barite accretion rate was calculated (see Appendix) and compared to the sedimentation rate at site GE99 32-2. All other parameters were set equal to those of the standard run (Tables 1 and 2). Model runs were stopped if steady-state conditions were met, if the total concentration of solids attained 70 wt% DS or if the benthic barite accretion rate exceeded the sedimentation rate, which is the necessary condition for barite chimney formation. A concentration of 70 wt% DS corresponds to a porosity of 0.2 and is a good approximation of the porosity remaining after the formation of a crust. In this set of runs we were able to reproduce a wide range of authigenic mineral distributions, ranging from pluri-metric sediment layers experiencing limited barite and calcium carbonate precipitation, to the formation of discrete crusts, as well as barite chimneys. In summary, we can distinguish three hydrological regimes giving rise to distinct diagenetic products:

5.2.1.1. Seepage rates from 0.14 to 20 cm a^{-1}. This interval of seepage rates results in dispersed calcium carbonate and barite precipitation throughout most of the sediment column. At the seepage rate of site GE99 32-2 (0.14 cm a^{-1}), precipitation rates of calcium carbonate and barite are relatively low (Fig. 6a) such that burial limits the maximum concentration of these minerals in the sediment column to a total of 5 wt% DS (Fig. 7). As the seepage rate is increased from 0.14 to 20 cm a^{-1}, the methane and barium fluxes from below increase, resulting in enhanced rates of AOM and HCO_3^- production, and of calcium carbonate and barite precipitation (Fig. 6a). Moreover, the precipitation depth decreases from roughly 280 cm to 140 cm and the total concentration of authigenic minerals in the sediment column increases. With a seepage rate of 5 cm a^{-1}, for example, up to 26 wt% of solids accumulate throughout the sediment column (Fig. 7). The microcrystalline precipitates and small-scale encrustations observed throughout sediment core GE99 32-2 were thus produced at seepage rates lower than 20 cm a^{-1}.

5.2.1.2. Seepage rates from 20 to 110 cm a^{-1}. At seepage rates greater than 20 cm a^{-1}, the depth-integrated rates of calcium carbonate and barite precipitation increase further (Fig. 6a), so that a discrete calcium carbonate/barite crust layer forms (Fig. 7). Following the steepening of solute concentration profiles with increasing seepage rates, the thickness of the crust decreases considerably at high seepage rates (~100 cm a^{-1}). Furthermore, following the increase in precipitation rates, the simulation time needed to form a crust layer falls from ~1000 yr with a seepage rate of 20 cm a^{-1}, to 50 yr with a seepage rate of 100 cm a^{-1}. It is therefore evident that sediments at site GE99 32-2 have been subject to a varying hydrological regime were low seepage rates of a few cm a^{-1} or less resulted in the precipitation of barite and calcium carbonate crystals, concretions, and coatings on worm tubes, whereas at least 2 distinct and persistent (several 100 yr long) events of more vigorous fluid expulsion (>20 cm a^{-1}) produced carbonate-barite crusts in the top 20 cm of the sediment column. Given that the present turnover rates at site GE99 32-2 do not promote crust formation, the two crusts present in this core have attained their position (115 and 210 cm depth) through burial.

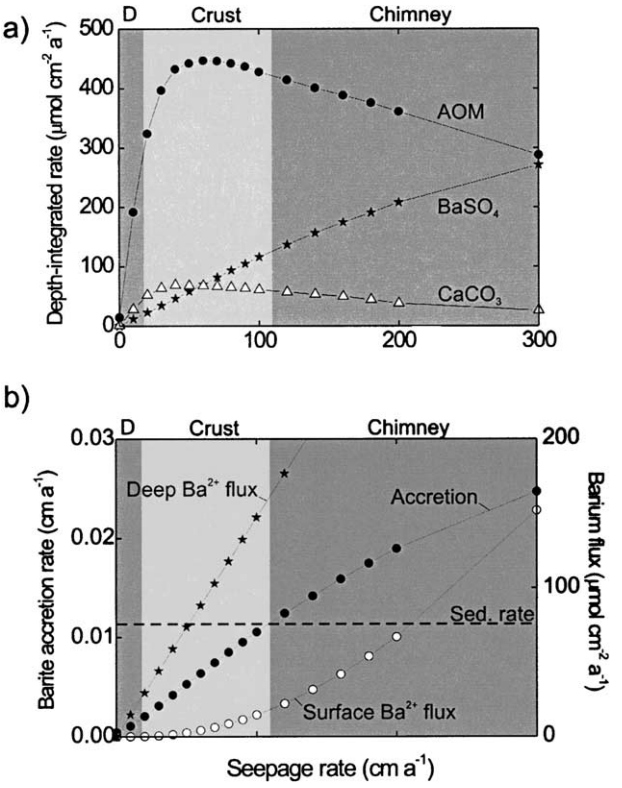

Fig. 6. Effect of varying the seepage rate on (a) the depth-integrated rates of biogeochemical reactions and (b) the benthic barite accretion rate and the barium flux to bottom waters. All other model parameters are set equal to those of the standard run (Tables 1 and 2). The shaded areas represent the hydrological regimes that result in dispersed diagenesis (D), formation of barite/calcium carbonate crusts (Crust) and barite chimneys (Chimney).

5.2.1.3. Seepage rates greater than 110 cm a^{-1}. At seepage rates greater than 110 cm a^{-1}, precipitation of calcium carbonate and barite takes place in close proximity to the upper boundary of the model column. Moreover, the vertical barite accretion rate becomes larger than the sedimentation rate (Fig. 6b), implying that the conditions for barite chimney formation are met. The precipitation regime has thus evolved from crust formation in the sediment, to chimney formation in the water column.

Accretion rates are not available for the barite chimneys of the Derugin Basin, so that the seepage rates responsible for their formation cannot be constrained based on our relation between seepage rate and benthic barite accretion rate (Fig. 6b). Nevertheless, our results indicate that at site GE99 32-2 barite chimney formation takes place if seepage rates exceed 110 cm a^{-1}.

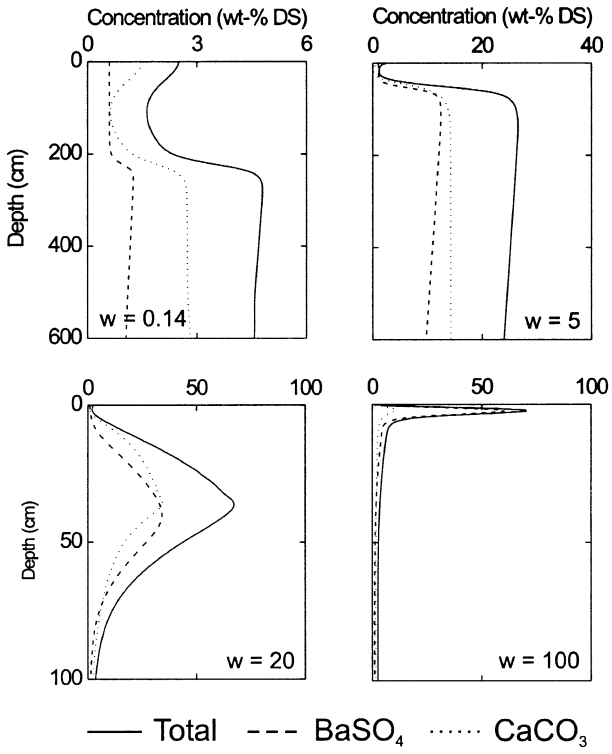

Fig. 7. Vertical distribution of authigenic barite and calcium carbonate in the sediment column at different seepage rates (w). All other model parameters are set equal to those of the standard run (Tables 1 and 2). Values of seepage rate in cm a^{-1}.

5.2.2. Controls on the mineralogy of authigenic precipitates

In this section we use the numerical model to identify the parameters which control the mineralogy of the authigenic precipitates formed at barium-rich cold seeps. We use the model runs of section 5.2.1 to address the question of why barite chimneys are devoid of authigenic carbonates; then we present the results of a second set of model runs we performed to investigate the controls on the mineralogy of sediment precipitates.

It is evident from the results of our first numerical experiment (section 5.2.1) that the seepage rate affects the precipitation rates of calcium carbonate and barite in different ways (Fig. 6a). Initially, both rates increase due to augmented Ba^{2+} and CH_4 fluxes from below. However, due to loss of methane through the establishment of a benthic methane flux, the integrated rate of AOM reaches a maximum at ~60 cm a^{-1}, and then declines. The limitation of bicarbonate production, as well as bicarbonate loss through a benthic flux, limit the rate of calcium carbonate precipitation which reaches a maximum at 50 cm a^{-1} and declines at higher seepage rates. In contrast, the depth-integrated rate of barite precipitation increases steadily in the investigated range of seepage rates (Fig. 6a). While bicarbonate availability is limited by the fate of methane, the availability of barium depends only on transport from below, so that for a given increase in the seepage rate, the saturation state with respect to barite increases more than that with respect to calcium carbonate. Since the precipitation rates of these minerals are proportional to the square of the saturation state (Table A2 in the Appendix), it follows that the precipitation kinetics of barite is more sensitive than that of calcium carbonate to increases in the seepage rate. Furthermore, as AOM rates diminish due to methane loss to bottom waters above 60 cm a^{-1}, increasing amounts of sulfate are available for barite precipitation, so that this mineral is favored over calcium carbonate at seepage rates greater than 60 cm a^{-1}. Consistent with the scarcity of calcium carbonate in the barite chimneys of the Derugin Basin (Greinert et al., 2002), in our model, the range of seepage rates resulting in chimney formation favor the precipitation of barite rather than calcium carbonate (Fig. 6a). In addition to the above, calcium carbonate precipitation in barite chimneys could be limited by microbial oxidation of AOM-derived sulfide, a process that decreases the pH and favors the dissolution of carbonates. Chemosynthetic tubeworms dependent on sulfide-oxidation have indeed been found living at the surface of barite chimneys (Greinert et al., 2002), rendering this hypothesis plausible. Given that, at seepage rates greater than 60 cm a^{-1}, the rate of calcium carbonate precipitation is inversely correlated to the seepage rate (Fig. 6a), our results likely explain the scarcity of authigenic carbonates also in barite chimneys at other cold seep sites, where elevated chimney accretion rates suggest that seepage rates in excess of 300 cm a^{-1} prevail (Naehr et al., 2000; Torres et al., 2002).

Precipitates formed in the sediment show a wide range of calcium carbonate/barite mixtures, regardless of the prevailing hydrological diagenetic regime, possibly indicating that a number of factors, in addition to the seepage rate, contribute in defining the mineralogy. To investigate this possibility, a second set of model runs was carried out varying the chemistry of the rising fluid within the range of fluid compositions found at cold seeps (Dia et al., 1993; Greinert et al., 2002; Torres et al., 2002; Luff and Wallmann, 2003). All runs were carried out at hydrological regimes favoring dispersed diagenesis (0.14 cm a^{-1}) and crust formation (20 cm a^{-1}). The effect of single parameter variations on the depth-integrated rates of AOM and of calcium carbonate and barite precipitation was monitored. The parameters that exert the strongest control on the ratio of precipitation rates are the concentrations of methane and barium at the base of the model column (Fig. 8). More specifically, as the methane concentration in the rising fluids is enhanced, AOM rates and HCO_3^- production increase. Thus, the depth-integrated rate of calcium carbonate precipitation is positively correlated to the methane concentration of deep fluids at both fluid flow regimes. Interestingly, the methane concentration of deep fluids also affects barium precipitation rates. At low methane concentrations ($C_{CH4}(L,t) < 5$–15 mM), barite precipitation rates are higher than those of calcium carbonate (Fig. 8). As the methane concentration increases, however, increased amounts of sulfate are consumed via AOM and are no longer available for barite precipitation. Thus, the rate of calcium carbonate precipitation exceeds that of barite precipitation at methane concentrations greater than 20 mM (Fig. 8). In the cold seep environment, barium is supplied nearly entirely by deep fluids. The rate of barite precipitation is thus positively correlated with the barium concentration in seep fluids at both seepage regimes (Fig. 8). In summary, the strongest control on the mineralogy of precipitates is exerted by the methane/barium ratio of seeping fluids. At relatively gentle seepage rates (0.14

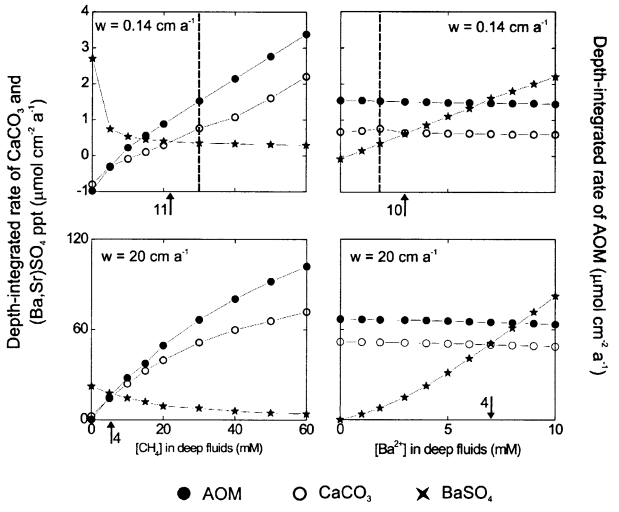

Fig. 8. Effect of varying the methane and barium concentration of the deep fluids on the depth-integrated rates of AOM and of calcium carbonate and barite precipitation. Model runs were conducted at two fluid seepage regimes (w = 0.14 cm a^{-1}, upper row and w = 20 cm a^{-1}, bottom row). Note: vertical dashed lines in the upper two graphs indicate the conditions of the standard run; arrows indicate conditions where barite and carbonate precipitation rates are equal, numbers next to arrows indicate the methane/barium ratio in these conditions.

cm a^{-1}) barite predominates if the methane/barium ratio is lower than ~11, while at high methane/barium ratios calcium carbonate is more abundant. At higher seepage rates (20 cm a^{-1}) the same trend exists but the threshold methane/barium ratio drops to ~4 (Fig. 8).

5.2.3. *Magnitude of barium fluxes to bottom waters*

To asses the impact of the different diagenetic regimes investigated in section 5.2.1 on barium fluxes to the water column, we calculated the barium flux at the base of the model column and compared it with the barium flux to bottom waters in the same set of model runs (Fig. 6b). As the seepage rate is enhanced from 0.14 to 300 cm a^{-1}, the barium flux at the base of the model column increases linearly by ~15 μmol cm^{-2} a^{-1} for every 10 cm a^{-1} of seepage rate, whereas the response of the barium flux to bottom waters is nonlinear (Fig. 6b). At the relatively low seepage rates which favor dispersed diagenesis (0.14 to 20 cm a-1) and extending into the field of crust formation (up to 40 cm a^{-1}), all of the dissolved barium in the rising fluids is consumed by precipitation in the sediment and no barium flux to bottom waters is produced. At seepage rates greater than 40 cm a^{-1}, however, a barium flux to bottom waters is established and is positively correlated to the seepage rate (Fig. 6b).

Based on the minimum seepage rate needed to form barite chimneys at site GE99 32-2 (110 cm a^{-1}), it follows that a minimum flux of barium to bottom waters of 20 μmol cm^{-2} a^{-1} is associated to barite chimney formation. Two lines of evidence suggest that this is a conservative estimate. Firstly, barium fluxes measured with benthic flux chambers placed in the vicinity of barite chimneys, but not on top of growing structures, at cold seeps in the Peru subduction zone (Torres et al., 1996a), in the Cascadia Margin (Torres et al., 2002) and in the San Clemente Basin (Torres et al., 2002) range from 23 μmol cm^{-2} a^{-1} to 182 μmol cm^{-2} a^{-1}. The highest value (182 μmol cm^{-2} a^{-1}) is 9 times larger than the calculated minimum flux associated to chimney formation (20 μmol cm^{-2} a^{-1}). Secondly, barite chimney accretion in other cold seep areas occurs at much greater rates (up to 1 cm a^{-1}) than the rate which produces our minimum model flux of 20 μmol cm^{-2} a^{-1} (0.011 cm a^{-1}) (Naehr et al., 2000; Torres et al., 2002). Given that the accretion rate is positively correlated to the barium flux to bottom waters (Fig. 6b), barite accretion rates comparable to those measured by Naehr et al. (2000) and Torres et al. (2002) would produce fluxes greatly in excess of our minimum estimate. More elevated fluxes would imply seepage rates higher than 110 cm a^{-1}, which indeed are a rather common occurrence at cold seeps where rates up to 1000 cm a^{-1} are routinely measured (Henry et al., 1992; Linke et al., 1994). Thus, we conclude that the flux of barium associated to barite chimney formation in the Sea of Okhotsk is very likely higher than 20 μmol cm^{-2} a^{-1}.

A conservative estimate of the cold seep barium flux from the Derugin Basin to bottom waters is possible by integrating the minimum flux estimate throughout the cold seep area. Considering that barite chimneys are distributed over an area of 22 km^2, and that they occupy 10% of the seafloor, if all chimneys are active, the barium flux to the water column is at least 4.4×10^5 mol a^{-1}. This value is 4 orders of magnitude smaller than the global hydrothermal barium flux of 3.35×10^9 mol a^{-1} (Dickens et al., 2003). Considering that the volume of water in the global ocean (~1.25×10^9 km^3), is 3 orders of magnitude greater than that of the Sea of Okhotsk (~1.2×10^6 km^3; Talley and Nagata, 1995) and that the flux of barium from the Derugin Basin is probably much greater than our minimum estimate of 4.4×10^5 mol a^{-1}, it is probable that barium release from the cold seeps of the Derugin Basin is of significance to barium cycling in the Sea of Okhotsk and, in particular, in the Derugin Basin, which experiences very limited exchange with the rest of the water masses of the Sea of Okhotsk (Freeland et al., 1998).

6. CONCLUSIONS

Biogeochemical processes at the barium-rich cold seeps of the Derugin Basin can be summarized as follows. Barium- and methane-rich, sulfate-free fluids are expelled along tectonic conduits giving rise to a giant cold seep. In the sediments, AOM dominates the biogeochemical turnover and exerts a strong control on both calcium carbonate and barite precipitation/dissolution processes. High amounts of dissolved barium, whose distribution in the pore fluids is controlled mainly by the concentration of sulfate, are rapidly consumed at the sulfate-methane boundary through precipitation of authigenic barite, which incorporates variable amounts of strontium. At comparable sediment depths, alkalinity production through AOM induces the precipitation of authigenic carbonates. The seepage rate exerts the main control on the type of authigenic mineral accumulation. At low seepage rates (~0.14 cm a^{-1}) precipitation of barite and calcium carbonate proceeds at relatively low depth-integrated rates (~20 μmol cm^2 a^{-1}) producing calcium carbonate and barite microcrystalline phases and concretions

throughout the top few meters of the sedimentary column. More vigorous fluid expulsion events (>20 cm a^{-1}) result in higher depth-integrated precipitation rates (up to ~60 μmol cm^2 a^{-1}) and promote the formation of discrete barite-carbonate layer in the uppermost 20 cm of the sediment column. The mineralogy of sediment precipitates is largely dependent on the chemistry of the expelled fluids. Thus, carbonates, whose rate of precipitation is directly related to the rate of AOM, prevail if the expelled fluids have elevated CH_4/Ba^{2+} ratios (>4–11) whereas barite dominates in fluids with lower CH_4/Ba^{2+} ratios. At seepage rates greater than 110 cm a^{-1}, barium reacts with seawater sulfate in bottom waters forming barite chimneys. Our results show that huge accumulations of barite can be formed by low-temperature seepage of barium- and methane-rich fluids, supporting recent propositions that some Paeleozoic stratiform barite deposits devoid of hydrothermal mineral assemblages were generated by cold seepage, rather than high temperature hydrothermal processes (Torres et al., in press). Moreover, a significant barium flux to bottom waters is associated to chimney formation in the Derugin Basin, supporting recent assumptions that massive events of cold seepage could have affected the marine barium cycle in the geological past (Dickens et al., 2003).

Acknowledgments—The captains and crew members of the research vessels *Akademik Lavrentyev* and M.S. *Gelovany* provided helpful assistance at sea, their work is greatly appreciated. We would like to thank N. Biebow for organizing the cruises. We are grateful to Jens Greinert for having provided the maps of the Derugin Basin area. A special thank goes to Bettina Domeyer, Anke Bleyer and Regina Surberg for having carried out the analytical work on board the *Akademik Lavrentyev* and at the shore based Geomar laboratories. We are grateful to two anonymous reviewers and to Gerald Dickens for having critically reviewed this manuscript. Funding for this study was provided by BMBF grant 03G0534A in the framework of the KOMEX project.

Associate editor: D. E. Canfield

REFERENCES

Aloisi G., Bouloubassi I., Heijs S. K., Pancost R. D., Pierre C., Sinninghe Damsté J. S., Gottschal J. C., Forney L. J., and Rouchy J.-M. (2002) CH_4-consuming microorganisms and the formation of carbonate crusts at cold seeps. *Earth Planet. Sci. Lett.* **203,** 195–203.

Astakhova N. V. (1993) Hydrothermal barite in the Okhotsk Sea. *Resour. Geol. Spec. Issue* **17,** 169–172.

Aquilina L., Dia A. N., Boulègue J., Bourgois J., and Fouillac A. M. (1997) Massive barite deposits in the convergent margin off Peru: Implications for fluid circulation within subduction zones. *Geochim. Cosmochim. Acta* **61,** 1233–1245.

Berner R. A. (1980) Early Diagenesis—A Theoretical Approach. Princeton University Press.

Biebow N., Lüdmann T., Karp R., Kulinich R. (2000) Cruise report: KOMEX III and IV (RV *Gagarinsky*; RV *Gelovany*). GEOMAR Report 88.

Bishop J. K. B. (1988) The barite-opal-organic carbon association in oceanic particulate matter. *Nature* **332,** 341–343.

Boetius A., Ravenschlag K., Schubert C. J., Rickert D., Widdel F., Gieske A., Amann R., Jørgensen B. B., Witte U., and Pfannkuche O. (2000) A marine microbial consortium apparently mediating anaerobic oxidation of methane. *Nature* **407,** 623–626.

Bogorov V. G. (1974) *Plankton of the World Ocean* (in Russian). Nauka.

Bollwerk S. M. (2002) Rezente submarine Barytbildung im Derugin Becken (Ochotskisches Meer). Ph.D. thesis. Christian Albrechts Universität, Kiel.

Boudreau B. P. (1997) *Diagenetic Models and Their Implementation*. Springer-Verlag.

Bosbach D. (2002) Linking molecular-scale barite precipitation mechanisms with macroscopic crystal growth rates. Geochemical Society, Houston. Special Publication. **7,** 97–110.

Burton E. A. and Walter L. M. (1987) Relative precipitation rates of aragonite and Mg calcite from seawater: Temperature or carbonate ion control? *Geology* **15,** 111–114.

Dehairs F., Chesselet R., and Jedwab J. (1980) Discrete suspended particles of barite and the barium cycle in the ocean. *Earth Planet. Sci. Lett.* **49,** 528–550.

Derkachev A. N., Bohrmann G., Greinert J., and Mozherovsky A. V. (2000) Authigenic calcite and barite mineralization in sediments from the Derugin basin (Sea of Okhohtsk) (in Russian). *Lithol. Miner. Resour.* **6,** 568–585.

Dia A. N., Aquilina L., Boulègue J., Bourgois J., Suess E., and Torres M. (1993) Origin of fluids and related barite deposits at vent sites along the Peru convergent margin. *Geology* **21,** 1099–1102.

Dickens G. R., Fewless T., Thomas E., and Bralower T. J. (2003) Excess barite accumulation during the Paleocene-Eocene Thermal Maximum: Massive input of dissolved baium from seafloor gas hydrate reservoirs. In *Causes and Consequences of Globally Warm Climates in the Early Paleogene* (eds. S. L. Wing, P. D. Gingerrich, B. Schmitz, and E. Thomas), pp.11–23. Special Paper 369. Geological Society of America.

Emerson S., Jahnke R., and Heggie D. (1984) Sediment-water exchange in shallow estuarine sediments. *J. Mar. Res.* **42,** 709–730.

Faugères J.-C., Gonthier E., Bobier C., and Griboulard R. (1997) Tectonic control on sedimentary processes in the southern termination of the Barbados Prism. *Mar. Geol.* **140,** 117–140.

Freeland H. J., Bychkov A. S., Whitney F., Taylor C., Wong C. S., and Yurasov G. I. (1998) WOCE section P1W in the Sea of Okhotsk 1. Oceanographic data description. *J. Geophys. Res.* **103,** 15,613–15,623.

Fu B., Aharon P., Byerly G. R., and Roberts H. H. (1994) Barite chimneys of the Gulf of Mexico slope: Initial report on their petrography and geochemistry. *Geo-Mar. Lett.* **14,** 81–87.

Greinert J., Bohrmann G., and Suess E. (2001) Methane venting and gas hydrate-related carbonates at the hydrate ridge: Their classification, distribution and origin. In *Natural Gas Hydrates: Occurence, Distribution, and Detection* (eds. C. K. Paull and W. P. Dillon), Vol. 124, pp. 99–113. Geophysics Monograph.

Greinert J., Bollwerk S. M., Derkachev A., Bohrmann G., and Suess E. (2002) Massive barite deposits and carbonate mineralization in the Derugin Basin, Sea of Okhotsk: Precipitation processes at cold seep sites. *Earth Planet. Sci. Lett.* **203,** 165–180.

Hales B. and Emerson S. (1997) Evidence in support of first-order dissolution kinetics of calcite in seawater. *Earth Planet. Sci. Lett.* **148,** 317–327.

Henry P., Foucher J.-P., Le Pichon X., Sibuet M., Kobayashi K., Tarits P., Chamot-Rooke N., Furuta T., and Schultheiss P. (1992) Interpretation of temperature measurements from the Kaiko-Nankai cruise: Modeling of fluid flow in clam colonies. *Earth Planet. Sci. Lett.* **109,** 355–371.

Iversen N. and Jørgensen B. B. (1985) Anaerobic methane oxidation rates at the sulfate-methane transition in marine sediment from Kattegat and Skagerrak (Denmark). *Limnol. Oceaonogr.* **30,** 944–955.

Kennedy H. A. and Elderfield H. (1987) Iodine diagenesis in pelagic deep-sea sediments. *Geochim. Cosmochim. Acta* **51,** 2489–2504.

Koblenz-Mischke O. J. (1967) Primary production of the Pacific Ocean (in Russian). In *Biology of the Pacific Ocean, Part 1* (ed. M. E. Vinogradov), pp. 62–65. Nauka.

Linke P., Suess E., Torres M., Martens V., Rugh W. D., Ziebis W., and Kulm L. D. (1994) In situ measurements of fluid flow from cold seeps at active continental margins. *Deep-Sea Res. I* **41,** 721–739.

Luff R., Wallmann K., Grandel S., and Schlüter M. (2000) Numerical modelling of benthic processes in the deep Arabian Sea. *Deep Sea Res. II* **47,** 3039–3072.

Luff R. and Wallmann K. (2003) Fluid flow, methane fluxes, carbonate precipitation and biogeochemical turnover in gas hydrate-bearing sediments at Hydrate Ridge, Cascadia Margin: Numerical modeling and mass balances. *Geochim. Cosmochim. Acta* **67,** 3403–3421.

Luff R., Wallmann K. and Aloisi G. (in press) Physical and biogeochemical constraints on carbonate crust formation at cold vent sites: Significance for fluid and methane budgets and chemosynthetic biological communities. *Earth Planet. Sci. Lett.*

Martin J., Gieskes J. M., Torres M., and Kastner M. (1993) Bromine and Iodine in Peru margin sediments and pore fluids: Implications for fluid origins. *Geochim. Cosmochim. Acta* **57,** 4377–4389.

McManus J., Berelson W. M., Klinkhammer G. P., Johnson K. S., Coale K. H., Anderson R. F., Kumar N., Burdige D. J., Hammond D. E., Brumsack H. J., McCorkle D. C., and Rushdi A. (1998) Geochemistry of barium in marine sediments: Implications for its use as a paleoproxy. *Geochim. Cosmochim. Acta* **62,** 3453–3473.

Naehr T., Stakes D., and Moore W. S. (2000) Mass wasting, ephemeral fluid flow, and barite deposition on the California continental margin. *Geology* **28,** 315–318.

Paull C. K., Chanton J. P., Neumann A. C., Coston J. A., and Martens C. S. (1992) Indicators of Methane-derived carbonates and chemosynthetic organic carbon deposits: Examples from the Florida escarpment. *Palaios* **7,** 361–375.

Paytan A., Mearon S., Cobb K., and Kastner M. (2002) Origin of marine barite deposits: Sr and S isotope charcterization. *Geology* **30,** 747–750.

Rushdi A. I., McManus J., and Colier R. W. (2000) Marine barite and celestite saturation in seawater. *Mar. Chem.* **69,** 19–31.

Suess E., Bohrmann G., von Huene R., Linke P., Wallmann K., Lammers S., and Sahling H. (1998) Fluid venting in the eastern Aleutian subduction zone. *J. Geophys. Res.* **103,** 2597–2614.

Talley L. D. and Nagata Y., eds. *The Okhotsk Sea and the Oyashio region. PICES Sci. Rep.* **2**, 227 pp, Sidney.

Torres M. E., Bohrmann G., and Suess E. (1996a) Authigenic barites and fluxes of barium associated with fluid seeps in the Peru subduction zone. *Earth Planet. Sci. Lett.* **144,** 469–481.

Torres M. E., Brumsack H. J., Bohrmann G., and Emeis K. C. (1996b) Barite fronts in continental margin sediments: A new look at barium remobilization in the zone of sulfate reduction and formation of heavy barites in diagenetic fronts. *Chem. Geol.* **127,** 125–139.

Torres M. E., McManus J., and Chih-An H. (2002) Fluid seepage along the San Clemente Fault scarp: Basin-wide impact on barium cycling. *Earth Planet. Sci. Lett.* **203,** 181–194.

Torres M. E., Bohrmann G., Dubé T. E. and Poole F. G. (In press) Formation of modern and stratiform barite at continental margin methane seeps. *Geology*.

U.S. Geological Survey (2003) Barite. USGS mineral commodity summary, 2003. USGS.

Van Cappellen P. and Wang Y. (1996) Cycling of iron and manganese in surface sediments: A general theory for the coupled transport and reaction od carbon, oxygen, nitrogen, sulfur, iron, and manganese. *Am. J. Sci.* **296,** 197–243.

Wallmann K., Linke P., Suess E., Bohrmann G., Sahling H., Schlüter M., Dählmann A., Lammers S., Greinert J. and von Mirbach. (1997) Quantifying fluid flow, solute mixing and biogeochemical turnover at cold vents of the eastern Aleutian subduction zone. *Geochim. Cosmochim. Acta* **61,** 5209–5219.

Zatsepina O. Y. and Buffet B. A. (1997) Phase equilibrium of gas hydrate: Implications for the formation of hydrate in the deep-sea floor. *Geophys. Res. Lett.* **24,** 1567–1570.

Zhong S. and Mucci A. (1993) Calcite precipitation in seawater using a constant addition technique: A new overall reaction kinetic expression. *Geochim. Cosmochim. Acta* **57,** 1409–1417.

A1. APPENDIX

The constant and variable parameter values used to describe the cold-seep sites in the Derugin Basin are summarized in Table A1. Starting from the initial concentration profiles for solutes and solids, the depth and time evolution of solid and solute concentrations is described by a set of 12 transport-reaction differential equations, one for each chemical species considered in the model, and is solved numerically by applying boundary conditions and the chosen parameter values. The differential equations for dissolved species (Eqn. 5) and solids (Eqn. 6) are based on the general diagenetic equations of Berner (1980), considering steady-state compaction and omitting bioturbation:

$$\frac{\partial(\phi(x)\cdot C_d(x,t))}{\partial t} = \frac{\partial}{\partial x}\left(D\cdot\phi^2(x)\cdot\frac{\partial C_d(x,t)}{\partial x}\right) - \frac{\partial(\phi(x)\cdot u(x)\cdot C_d(x,t))}{\partial x} + \phi(x)\cdot BIO(x)\cdot(C_0 - C_d(x,t)) + \phi(x)\cdot\sum R_d(x,t) \quad (5)$$

$$\frac{\partial((1-\phi(x))\cdot C_s(x,t))}{\partial t} = -\frac{(1-\phi_f)\cdot v_f\cdot\partial(C_s(x,t))}{\partial x} + (1-\phi(x))\cdot\sum R_s(x,t) \quad (6)$$

where C_d is the concentration of solutes in μmol (cm^3 pore fluids)$^{-1}$ (hereafter μmol cm^{-3}), C_s is the concentration of solids in wt% dry sediment (hereafter wt% DS), D, in cm^2 a^{-1}, is the molecular diffusion coefficient, and ΣR_d, in μmol (cm^3 pore fluid)$^{-1}$ a^{-1} (hereafter μmol cm^{-3} a^{-1}) and ΣR_s, in wt% DS a^{-1}, are the rates of all diagenetic reactions affecting dissolved and solid species, respectively. Precipitation rates of $CaCO_3$ and $(Ba,Sr)SO_4$ are computed in μmol cm^{-3} a^{-1}, whereas dissolution rates of these minerals are computed in wt% DS a^{-1}. Where necessary, the unit conversion functions f_{Ca} and f_{Ba} (Table A3) are used to convert the units of precipitation and dissolution rates into those of the reaction terms of the differential equations (Eqn. 5 and 6). The reaction terms are defined in Table A4.

The system of 12 differential equations is solved using finite difference techniques as implemented in the commercial software MATHEMATICA. The object NDSolve which was applied to integrate the differential equations uses the numerical Method of Lines. This procedure based on partial discretization has been used successfully in previous modeling of benthic processes (Boudreau, 1997; Luff et al., 2000). A typical model run was completed within 1 h of computation time on a PC with Pentium IV processor. In the majority of the runs conditions approaching steady-state for solute concentrations are attained in less than 1000 yr of simulation time, while solids require a longer time which is strongly dependent on the chosen sedimentation rate.

A1.1. Porosity

The porosity-depth distribution in the sediment is considered to be produced by steady-state compaction (Berner, 1980) and is described by the following exponential function:

$$\phi(x) = \phi_f + (\phi_0 - \phi_f)\cdot e^{[-\phi_a\cdot x]} \quad (7)$$

where values of porosity at the sediment surface (ϕ_0), porosity at great sediment depth (ϕ_f) and of the porosity-depth attenuation coefficient (ϕ_a) have been determined for the studied sites by fitting porosity data obtained by the measurement of the sediment water content.

A1.2 Transport Processes

The numerical description of diffusion, advection and bioirrigation processes is based on the general diagenetic equations of Berner (1980). Molecular diffusion coefficients for the solute species (Table A1) are taken from Boudreau (1997). The effect of tortuosity on diffusion coefficients is accounted for by applying Archie's law (Berner, 1980).

Because fine grained sediments undergo compaction soon after sedimentation, the advection of solids at a given depth (i.e., the velocity of downwards flow of bulk solids relative to the seafloor), is equal to the rate of burial, or sedimentation rate, v_f, modified by compaction (Berner, 1980). The formulation used in the differential equations for solids species is valid for steady state compaction (Berner, 1980).

At cold seeps, the rate of fluid advection through the sediment column is composed of the downward burial component modified by compaction and the upward component due to fluid advection. In the

Table A1. Constant and variable parameter values used to describe the cold seep sites in the Derugin Basin.[a]

Parameter	Symbol	Value	Unit
Constant parameters			
Temperature	T	2.1	°C
Average density of dry solids	d_s	2.6	g cm^{-3}
Density of barite	d_s^{Ba}	4.48	g cm^{-3}
Porosity of barite chimneys	ϕ_{Ba}	0.4	—
Solubility constant for calcite in seawater	KC_{sp}	604.8	(μmol cm^{-3})^2
Solubility constant for barite in seawater	KB_{sp}	7.167×10^{-3}	(μmol cm^{-3})^2
Molecular diffusion coefficient for Ca^{2+}	$D_{Ca^{2+}}$	125	cm^2 a^{-1}
Molecular diffusion coefficient for Ba^{2+}	$D_{Ba^{2+}}$	139	cm^2 a^{-1}
Molecular diffusion coefficient for Sr^{2+}	$D_{Sr^{2+}}$	127	cm^2 a^{-1}
Molecular diffusion coefficient for SO_4^{2-}	$D_{SO_4^{2-}}$	169	cm^2 a^{-1}
Molecular diffusion coefficient for HS^-	D_{HS^-}	346	cm^2 a^{-1}
Molecular diffusion coefficient for CH_4	D_{CH_4}	314	cm^2 a^{-1}
Molecular diffusion coefficient for HCO_3^-	$D_{HCO_3^-}$	177	cm^2 a^{-1}
Molecular diffusion coefficient for CO_2	D_{CO_2}	313	cm^2 a^{-1}
Molecular diffusion coefficient for I^-	D_{I^-}	338	cm^2 a^{-1}
Bottom water Ca^{2+} concentration	C_{CaBW}	10.5	μmol cm^{-3}
Bottom water Ba^{2+} concentration	C_{BaBW}	2.48×10^{-4}	μmol cm^{-3}
Bottom water Sr^{2+} concentration	C_{SrBW}	0.078	μmol cm^{-3}
Bottom water HCO_3^- concentration	C_{HCO3BW}	2.4	μmol cm^{-3}
Bottom water CO_2 concentration	C_{CO2BW}	0.1	μmol cm^{-3}
Bottom water HS^- concentration	C_{HSBW}	0	μmol cm^{-3}
Bottom water CH_4 concentration	C_{CH4BW}	0	μmol cm^{-3}
Bottom water SO_4^{2-} concentration	C_{SO4BW}	28.9	μmol cm^{-3}
Bottom water I^- concentration	C_{IBW}	7×10^{-4}	μmol cm^{-3}
Variable parameters			
Length of the model column	L	variable	cm
Sedimentation rate at great depth	v_f	variable	cm a^{-1}
Bioirrigation coefficient at the surface	BIO0	variable	a^{-1}
Halving depth of bioirrigation	xs	variable	cm
Advective fluid flow at the seafloor	W_0	variable	cm a^{-1}
Mole fraction $SrSO_4$ in pre-existing barite	f_{Srpb}	variable	—
Fluid-barite Sr partition coefficient	P_C	variable	—
Depth of top of barite debris layer	x_0	variable	cm
Steepness factor at top of barite debris layer	d_x	variable	cm
Initial barite concentration in sediment	$(Ba,Sr)SO_{4_{sed}}$	variable	wt-% DS
Barite concentration in debris layer	C_{dl}	variable	wt-% DS

[a] DS = dry sediment.

Table A2. Rate equations.[a]

Process	Rate expression
AOM	$R_{AOM}(x,t) = k_{AOM} \cdot C_{SO_4^{2-}}(x,t) \cdot C_{CH_4}(x,t)$
CPD	$R_{CPPT}(x,t) = k_{CPPT} \cdot (\Omega_C(x,t) - 1)^2$
	$R_{CDISS}(x,t) = k_{CDISS} \cdot C_{CaCO_3}(x,t) \cdot (\Omega_C(x,t) - 1)$
	$R_C(x,t) = H[(\Omega_C - 1)] \cdot R_{CPPT}(x,t) + H[-(\Omega_C - 1)] \cdot f_C(x) \cdot R_{CDISS}(x,t)$
BPD	$R_{BPPT}(x,t) = k_{BPPT} \cdot (\Omega_B(x,t) - 1)^2$
	$R_{BDISS}(x,t) = k_{BDISS} \cdot C_{(Ba,Sr)SO_4}(x,t) \cdot (\Omega_B(x,t) - 1)$
	$R_B(x,t) = H[(\Omega_B - 1)] \cdot R_{BPPT}(x,t) + H[-(\Omega_B - 1)] \cdot f_B(x) \cdot R_{BDISS}(x,t)$
	$R_{Ba}(x,t) = H[(\Omega_B - 1)] \cdot R_{BPPT}(x,t) \cdot \left(\frac{C_{BaSO_4}(x,t)}{C_{(Ba,Sr)SO_4}(x,t)}\right)_{solid} + H[-(\Omega_B - 1)] \cdot f_B(x) \cdot R_{BDISS}(x,t) \cdot \frac{C_{BaSO_4}(x,t)}{C_{(Ba,Sr)SO_4}(x,t)}$
	$R_{Sr}(x,t) = H[(\Omega_B - 1)] \cdot R_{BPPT}(x,t) \cdot \left(\frac{C_{SrSO_4}(x,t)}{C_{(Ba,Sr)SO_4}(x,t)}\right)_{solid} + H[-(\Omega_B - 1)] \cdot f_B(x) \cdot R_{BDISS}(x,t) \cdot \frac{C_{SrSO_4}(x,t)}{C_{(Ba,Sr)SO_4}(x,t)}$
BCF	$R_{BAC} = \frac{\sum_{x=0}^{x=L} R_{BPPT}(x,t_{max})}{d_s^{Ba} \cdot \phi_{Ba}}$

[a] AOM = anaerobic oxidation of methane; CPD = calcite precipitation/dissolution; BDP = barite precipitation/dissolution; BCF = barite chimney formation.

Table A3. Unit conversion functions.[a]

Parameter	From units	To units	Function
R_{CDISS}	$\frac{wt\%DS}{a}$	$\frac{\mu mol}{cm^3 \cdot a}$	$f_C(x) = \frac{10 \cdot d_s \cdot (1-\phi(x))}{0.1 \cdot \phi(x)}$
R_{BDISS}	$\frac{wt\%DS}{a}$	$\frac{\mu mol}{cm^3 \cdot a}$	$f_B(x) = f_C(x) \cdot \left(\frac{100}{233}\right)$
R_{CPPT}	$\frac{\mu mol}{cm^3 \cdot a}$	$\frac{wt\%DS}{a}$	$1/f_C(x)$
R_{BPPT}	$\frac{\mu mol}{cm^3 \cdot a}$	$\frac{wt\%DS}{a}$	$1/f_B(x)$

[a] DS = dry sediment.

model we follow the mathematical treatment of Luff and Wallmann (2003):

$$u(x) = \frac{v_f \cdot \phi_f - w_0 \cdot \phi_0}{\phi(x)} \quad (8)$$

where v_f is the sedimentation rate at great depth and w_0 the upwards rate of fluid flow at the seafloor (other parameters refer to the shape of the porosity profile, see Eqn. 7). Eqn. 8 is used in the advection term of the differential equations for solutes (Eqn. 5).

Bioirrigation, the pumping activity of benthic mega- and macrofauna, is described as a non local mixing, in which porewater is exchanged with bottom water over a relatively long vertical distance in the surface sediment by benthic infauna (Emerson et al., 1984). In the model nonlocal mixing is expressed by a source/sink term:

$$R_b = BIO(x) \cdot (C_{dBW} - C(x,t)) \quad (9)$$

where C_{dBW} is the bottom water concentration of a given solute and C(x,t) is the concentration of the same solute at depth x and time t. The decrease of bioirrigation intensity with depth in the sediment follows a gaussian decrease law:

$$BIO(x) = \frac{BIO0}{1 + e^{(x-x_s)/20}} \quad (10)$$

where BIO0 is the bio-irrigation at zero depth, in a^{-1}, and x_s is the halving depth of bio-irrigation, in cm. Thus, BIO0 has dimensions of frequency and is a measure of the intensity of bioirrigation, while x_s has dimensions of length and controls the depth of sediment that is affected by bioirrigation.

A1.3 Boundary Conditions, Benthic Barite Accretion Rate and Fluxes of Barium to Bottom Waters

Marine sediments are covered by rapidly flowing turbulent bottom waters. Closely above the sediment surface, lateral water flow and eddy diffusion are strongly diminished due to friction so that diffusive processes dominate the vertical solute transport. This so called diffusive boundary layer extends typically ~1 mm into the overlying bottom water (Boudreau, 1997). At cold vent sites, the transport of dissolved species through this layer and into the overlying water column is controlled by diffusion at seepage rates smaller than 2000 cm a^{-1} (Linke et al., in preparation). The fluxes of dissolved species across the upper boundary of the model column (at x = 0) are thus defined by the following equation which is also used as upper boundary condition for the modeling of pore water profiles:

$$-\phi_0 \cdot D_s \cdot \left(\frac{\partial C_d}{\partial x}\right)_{0,t} + \phi_0 \cdot u(0) \cdot C_d(0,t) = D_s \cdot \frac{C_d(0,t) - C_{dBW}}{zd} \quad (11)$$

where ϕ_0 is the sediment porosity at zero depth, $u(0)$, calculated with Eqn. 8, is the seepage rate at the seafloor, $C_d(0,t)$ is the concentration at zero depth, C_{dBW} is the solute concentration prevailing in the overlying bottom water and zd is the thickness of the diffusive boundary layer (0.1 cm). By using Eqn. 11, the concentration of solutes at the upper boundary is free to vary depending on the prevailing chemical and hydrological conditions. Thanks to this treatment, the model is able to correctly calculate the precipitation rate of barite at high seepage rates, where the high dissolved barium fluxes from below produces supersaturation with respect to barite at zero depth, and barite chimneys develop. In these conditions, the vertical benthic barite accretion rate, R_{BAC}, in cm a^{-1}, is calculated as the ratio of the depth-integrated barite precipitation rate at t_{max}, in μmol cm^{-2} wet sediment a^{-1}, to the density of barite chimneys, approximately equal to 2.5 g cm^{-3} (=10970 μmol (Ba,Sr)SO_4 cm^{-3}) for a porosity of 0.4 (Table A4). In addition, the flux of barium at x = 0 calculated with Eqn. 11 corresponds to the flux of barium to the water column, in the complete span of diagenetic regimes ranging from sediment precipitation to barite chimney formation.

At the base of the sediment column, concentrations are determined by the composition of the rising vent fluids.

A1.4 Biogeochemical Reactions

The model considers a simplified version of the DIC system and calcium carbonate precipitation/dissolution processes which are described by Eqn. 2. The total dissolved inorganic carbon, DIC, is thus calculated as:

$$DIC(x,t) = C_{CO_2}(x,t) + C_{HCO_3^-}(x,t) \quad (12)$$

The degree of carbonate saturation, Ω_C, is expressed by:

$$\Omega_C(x,t) = \frac{C_{Ca^{2+}}(x,t) \cdot C_{HCO_3^{-2}}(x,t)}{C_{CO_2}(x,t) \cdot KC_{sp}} \quad (13)$$

where KC_{sp}, the solubility constant for calcite in seawater, is formulated in such a way that at the upper boundary $\Omega_C = 1$ and no precipitation or dissolution takes place:

$$KC_{sp} = \frac{C_{Ca^{2+}}(0,t) \cdot C^2_{HCO_3^-}(0,t)}{C_{CO_2}(0,t)} \quad (14)$$

The rising fluids are considered to be in equilibrium with solid calcium carbonate. The lower boundary condition for CO_2 is thus formulated in such a way that $\Omega_C = 1$ also at the lower boundary:

$$C_{CO_2}(L,t) = \frac{C_{Ca^{2+}}(L,t) \cdot C^2_{HCO_3^-}(L,t)}{KC_{sp}} \quad (15)$$

Bicarbonate is produced through anaerobic oxidation of methane (Eqn. 1). The rate equation of this reaction is formulated following Van Cappellen and Wang (1996), where the rate, R_{AOM}, is proportional to the concentration of both methane and sulfate (Table A2). The total alkalinity, TA, is calculated as:

Table A4. Reaction terms used in the differential equations for solute (Eqn. 5) and solid (Eqn. 6) species.

Species	Reaction term
Ca^{2+}	$\Sigma R_{Ca^{2+}}(x,t) = -R_C(x,t)$
Ba^{2+}	$\Sigma R_{Ba^{2+}}(x,t) = -R_{Ba}(x,t)$
Sr^{2+}	$\Sigma R_{Sr^{2+}}(x,t) = -R_{Sr}(x,t)$
HCO_3^-	$\Sigma R_{HCO_3^-}(x,t) = +R_{AOM}(x,t) - 2 \cdot R_C(x,t)$
CO_2	$\Sigma R_{CO_2}(x,t) = +R_C(x,t)$
CH_4	$\Sigma R_{CH_4}(x,t) = -R_{AOM}(x,t)$
HS^-	$\Sigma R_{HS^-}(x,t) = +R_{AOM}(x,t)$
SO_4^{2-}	$\Sigma R_{SO_4^{2-}}(x,t) = -R_{AOM}(x,t) - R_B(x,t)$
$CaCO_3$	$\Sigma R_{CaCO_3}(x,t) = +R_C(x,t)/f_C(x)$
$(Ba,Sr)SO_4$	$\Sigma R_{(Ba,Sr)SO_4}(x,t) = +R_B(x,t)/f_B(x)$
$SrSO_4$	$\Sigma R_{SrSO_4}(x,t) = +R_{Sr}(x,t)/f_B(x)$

$$TA(x,t) = C_{HCO_3^-}(x,t) + C_{HS^-}(x,t) \quad (16)$$

The precipitation rate of calcium carbonate, R_{PPT}, is assumed to be proportional to the square of the saturation state (Table A2). In laboratory experiments various authors have observed a nonlinear dependence on saturation state resulting in exponents ranging from 0.4 to 2.8 (Burton and Walter, 1987; Zhong and Mucci, 1993). In our case, an exponent equal to 2 best describes our biogeochemical data set. The rate of calcium carbonate dissolution, R_{CDISS}, is assumed to depend linearly on saturation state and to be proportional to the amount of calcium carbonate present in the sediment column (Table A2) (Hales and Emerson, 1997).

The model considers the precipitation of barite. The degree of barite saturation, Ω_B, is expressed as:

$$\Omega_B(x,t) = \frac{C_{SO_4^{2-}}(x,t) \cdot C_{Ba^{2+}}(x,t)}{KB_{sp}} \quad (17)$$

The rate of barite precipitation, R_{BPPT}, is assumed be proportional to the square of the saturation state (Table A2) as observed in laboratory experiments (Bosbach, 2002). The rate of barite dissolution, R_{BDISS}, is formulated in a similar way to that of calcite and is assumed to depend linearly on saturation state and to be proportional to the amount of barite present in the sediment column (Table A2).

To investigate a possible effect of barite chimney debris in core GE99 32-2 on the considered biogeochemical processes, the initial concentration of barite in the sediment is described by a Boltzman function:

$$(Ba,Sr)SO_{4i(x)} = C_{dl} + \frac{(Ba,Sr)SO_{4_{sed}} - C_{dl}}{1 + e^{(x-x_0)/d_x}} \quad (18)$$

This function creates a step in the initial barite concentration profile and allows controlling its position and shape by varying the parameters C_{dl}, the concentration of barite in the debris layer, x_0, the depth of the top of the layer and d_x, the steepness of the barite profile at the top of the layer. $(Ba,Sr)SO_{4sed}$, the background concentration of barite in the sediment, is used as the upper boundary concentration for barite.

The expressions for precipitation and dissolution of a given mineral are combined obtaining the expressions R_C and R_B which describe precipitation/dissolution processes for calcium carbonate and barite (Table A2). In these expressions, H, the Heaviside function, is equal to 0 if its argument is negative and equal to 1 if its argument is equal to 0 or is positive. Thus, this formulation allows for precipitation when fluids are supersaturated and dissolution when fluids are undersaturated. Expressions R_C and R_B are introduced in the reaction term for the relevant chemical species (Table A4).

Sr^{2+} is allowed to coprecipitate with Ba^{2+} in barite. To account for this, the $SrSO_4$ species has been introduced in the model. Thus, the concentration of barite is the sum of the concentrations of $SrSO_4$ and $BaSO_4$ that compose the solid solution:

$$C_{(Ba,Sr)SO_4}(x,t) = C_{BaSO_4}(x,t) + C_{SrSO_4}(x,t) \quad (19)$$

The $SrSO_4$ species does not represent the strontium sulfate mineral Celestite, but rather the Sr substituting Ba in barite. Thus, its thermodynamic stability and rate of precipitation are proportional to those of barite through the mole fraction of $SrSO_4$ precipitating in barite calculated with Eqn. 24 (Table A2). The boundary condition for the $SrSO_4$ species is based on the mole fraction $SrSO_4$ in the preexisting barite, f_{Srpb}:

$$C_{SrSO_4}(0,t) = f_{Srpb} \cdot (Ba,Sr)SO_{4_{sed}} \quad (20)$$

In addition, the initial concentration profile for the $SrSO_4$ species is proportional to the initial barite concentration such that the Sr content of the preexisting barite is constant with depth also when considering the presence of a barite debris layer.

The Sr/Ba ratio in precipitating barite is proportional to the Sr/Ba ratio of the diagenetic fluids:

$$\left(\frac{C_{SrSO_4}(x,t)}{C_{BaSO_4}(x,t)}\right)_{solid} = \frac{1}{P_C} \cdot \frac{C_{Sr^{2+}}(x,t)}{C_{Ba^{2+}}(x,t)} \quad (21)$$

where P_C is the Sr fluid-solid partition coefficient and the subscript *solid* refers to the composition of the precipitating barite. Thus, barite precipitation consumes Ba^{2+} and Sr^{2+} in a proportion which depends on the partition coefficient and on the Sr^{2+}/Ba^{2+} ratio of the diagenetic fluid. To correctly compute changes in the Sr and Ba composition of fluid and barite, the mole fractions of $BaSO_4$ and $SrSO_4$ in the precipitating barite have to be expressed in terms of the $(SrSO_4/BaSO_4)_{solid}$ term computed with Eqn. 21, and introduced in the expressions for the rate of Ba^{2+} and Sr^{2+} consumption during barite precipitation (Table A2). This calculation proceeds as follows. The term on the left of Eqn. 21 can be expressed as:

$$\left(\frac{C_{SrSO_4}(x,t)}{C_{BaSO_4}(x,t)}\right)_{solid} = \left(\frac{C_{SrSO_4}(x,t)}{C_{(Ba,Sr)SO_4}(x,t) - C_{SrSO_4}(x,t)}\right)_{solid} \quad (22)$$

Rearranging Eqn. 22 we obtain the expression of the mole fraction of $SrSO_4$ in precipitating barite:

$$\left(\frac{C_{SrSO_4}(x,t)}{C_{(Ba,Sr)SO_4}(x,t)}\right)_{solid} = \left(\frac{C_{SrSO_4}(x,t)}{C_{BaSO_4}(x,t)}\right)_{solid} \Big/ 1 + \left(\frac{C_{SrSO_4}(x,t)}{C_{BaSO_4}(x,t)}\right)_{solid} \quad (23)$$

Substituting Eqn. 21 in Eqn. 23, we obtain

$$\left(\frac{C_{SrSO_4}(x,t)}{C_{(Ba,Sr)SO_4}(x,t)}\right)_{solid} = \frac{C_{Sr^{2+}}(x,t)}{P_C \cdot C_{Ba^{2+}}(x,t) + C_{Sr^{2+}}(x,t)} \quad (24)$$

By difference, we obtain the expression for the mole fraction of $BaSO_4$ in precipitating barite:

$$\left(\frac{C_{BaSO_4}(x,t)}{C_{(Ba,Sr)SO_4}(x,t)}\right)_{solid} = 1 - \frac{C_{Sr^{2+}}(x,t)}{P_C \cdot C_{Ba^{2+}}(x,t) + C_{Sr^{2+}}(x,t)} \quad (25)$$

The mole fractions of $BaSO_4$ and $SrSO_4$ in precipitating barite, calculated with Eqn. 24 and 25, are introduced in the expressions for the rate of Ba^{2+} and Sr^{2+} consumption during barite precipitation (Table A2). In these rate expressions the Heaviside function, H, allows for production of Ba^{2+} and Sr^{2+} during dissolution of barite and consumption of Ba^{2+} and Sr^{2+} during barite precipitation; these expressions correctly compute the changes in the Sr/Ba ratio of the diagenetic fluids and of barite during these processes.